Eur. Phys. J. A **6**, 167–174 (1999)

THE EUROPEAN PHYSICAL JOURNAL A

In-beam γ-spectroscopy with relativistic radioactive ion beams

S. Wan[1], J. Gerl[1,a], J. Cub[6], J.M. Holeczek[7], P. Reiter[5], D. Schwalm[2], T. Aumann[1], K. Boretzky[4], W. Dostal[4], B. Eberlein[4], H. Emling[1], Ch. Ender[2], Th.W. Elze[3], H. Geissel[1], A. Grünschloß[3], R. Holzmann[1], N. Iwasa[1], M. Kaspar[1,3], A. Kleinböhl[1,3], O. Koschorrek[2], Y. Leifels[1], A. Leistenschneider[3], I. Peter[1], H. Schaffner[1], C. Scheidenberger[1], R. Schubart[1], R. Schubert[1,3], H. Simon[6], G. Stengel[3], A. Surowiec[1], H.J. Wollersheim[1]

[1] Gesellschaft für Schwerionenforschung, Planckstrasse 1, 64291 Darmstadt, Germany
[2] Max-Planck-Institut für Kernphysik, Postfach 103980, 69029 Heidelberg, Germany
[3] Institut für Kernphysik, Universität Frankfurt, 60486 Frankfurt, Germany
[4] Institut für Kernchemie, Universität Mainz, 55029 Mainz, Germany
[5] Sektion Physik der LMU München, Am Coulombwall 1, 85748 Garching, Germany
[6] Institut für Kernphysik, Technische Universität Darmstadt, 64289, Germany
[7] Instytut Fizyki, Uniwersytet Śląski, 40-007 Katowice, Poland

Received: 2 August 1999
Communicated by B. Povh

Abstract. This work demonstrates the feasibility of in-beam γ-spectroscopy employing radioactive ion beam species at relativistic energies of E = 210 $\sim$ 280 A·MeV. Neutron-rich nuclei below ^{48}Ca with neutron number between the two magic numbers 20 and 28 have been investigated. Using a Pb target, single step inelastic excitation originating mainly from Coulomb interaction takes place populating preferentially low-lying low-spin states and enabling the extraction of B(E2) values. On a C target, nucleon removal reactions are dominating and medium-spin states are populated thus offering spectroscopic information in neighboring nuclei. Cross sections of inelastic excitation are determined and compared to coupled-channels calculations. Two new states of the very neutron-rich nucleus ^{44}Ar at 1.78(8) MeV and 2.61(16) MeV are deduced from γ-transitions.

PACS. 25.60.+v reactions induced by unstable nuclei – 25.75.+r relativistic heavy ion collisions – 23.20.Lv gamma transitions and level energies – 27.40.+z $39 < A < 58$ – 29.30.Kv X- and γ-ray spectroscopy

1 Motivation

In-beam γ-spectroscopy with relativistic (E>200 A·MeV) radioactive ion beams (RIB) is a rather untouched field [1,2] which offers new opportunities to study the nuclear structure of exotic nuclei: Coulomb excitation and few nucleon removal reactions provide rich spectroscopic information; thick secondary targets can be used resulting in large yields counteracting low beam intensities. On the other hand, one has to cope with large Doppler effects and huge atomic background. The aim of this work is to demonstrate the feasibility of this new experimental method by studying the nuclear structure of neutron-rich nuclei below ^{48}Ca. The reason to choose this region with neutron numbers around the two magic numbers 20 and 28 is the observed unexpectedly large deformation of ^{32}Mg [3], which has triggered new shell model calculations in this mass region with detailed predictions concerning the stability of the magic neutron shell closures against deformation.

[a] e-mail: j.gerl@gsi.de

2 Experiment

The experiment was performed at GSI, Darmstadt. After the fragmentation reaction of ^{50}Ti on a 4 g/cm^2 ^{9}Be production target at 330 A·MeV, about 50 nuclear species (in which more than 30 were β-unstable neutron-rich isotopes) with charge numbers of 4 $\sim$ 20, mass-to-charge ratios of 2.1 $\sim$ 2.5 and energies of 210 $\sim$ 280 A·MeV ($\beta \equiv v/c = 0.58 \sim 0.64$) were selected simultaneously by the FRagment Separator FRS. This secondary RIB was transferred to the target area and had an intensity of around 10^4 particles per second (pps) for the full beam which corresponds to an average of about 200 pps for each nuclear species.

The experimental set-up at the target area is shown in Fig. 1. Secondary peripheral reactions of the RIB with a 0.94 g/cm^2 Pb and a 0.54 g/cm^2 C target were employed to populate excited states. The γ-rays emitted from reaction products were measured by a 4π γ-spectrometer, the Darmstadt-Heidelberg Crystal Ball (CB) consisting of 153 individual NaI crystals with an intrinsic energy resolution

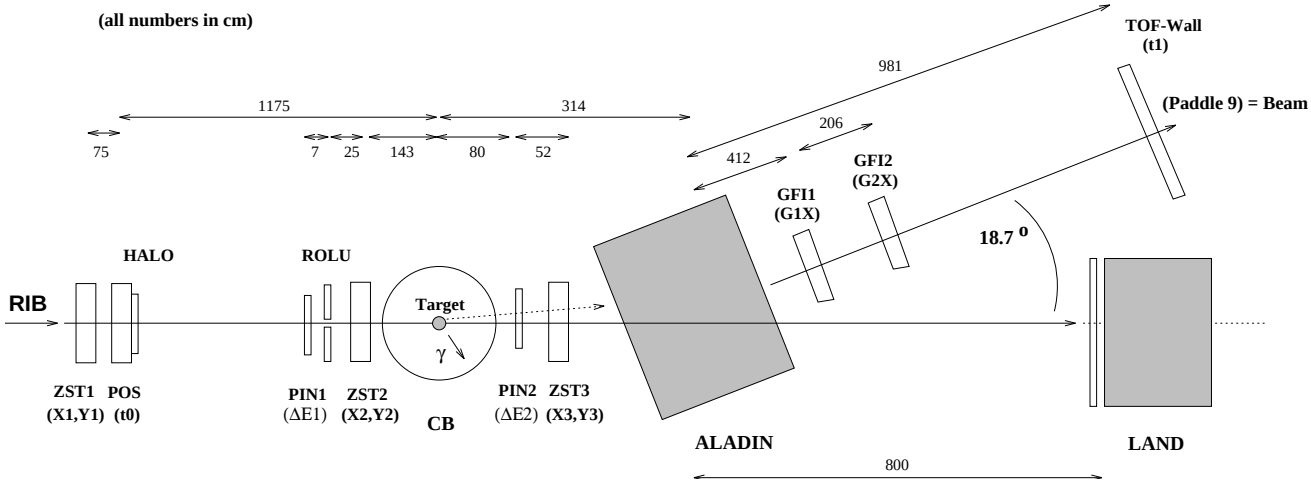

Fig. 1. Schematic set-up for the ^{50}Ti experiment at the target area with distances given in cm

of 7% and a full energy efficiency of 56% at 1408 keV [4,5].

Two plastic scintillators were used to veto the beam halo: HALO, which is a 10×10 cm^2 square with a $\phi = 8$ cm circular hole and ROLU, which is composed of four plastic bars forming a rectangular hole which can be adjusted from 0×0 to 4×4 cm^2 by moving the bars along a frame [6]. During most of the beam time, ROLU was set to 3×3 cm^2 opening area which gave the limit of the usable beam size at the target position.

In order to identify nuclear species in the RIB on an event by event basis and to distinguish different reaction channels, charge and mass number Z_i and A_i were measured, with i=1 and 2 corresponding to before and behind the target, respectively.

Z_1 and Z_2 were determined by two ΔE counters (PIN1 and PIN2) which consisted of 0.17 mm thick silicon PIN diodes of 5×5 cm^2 size and close to 100% efficiency.

As the particles were fully ionized, the mass number A_i can be derived from Z_i, velocity β_i and magnetic rigidity $(B\rho)_i$ with the relation $B\rho = \frac{p}{Ze} \propto \frac{A}{Z}\frac{\beta}{\sqrt{1-\beta^2}}$. As the energy loss in the thick Pb- and C-target was mainly due to atomic processes, with an iterative calculation [5], β_1 and β_2 were derived from the time of flight between two plastic scintillators: POS with a diameter of 10 cm and a time resolution of ∼100 ps and the TOF-wall with 208×200 cm^2 size and 200∼300 ps time resolution. With its 20 scintillator paddles arranged parallel to each other along the vertical direction, the TOF-wall can also give position information with a resolution of 10 cm (horizontal) and 2∼3 cm (vertical). With $(B\rho)_1 = 5.588$ Tm and $\Delta(B\rho)_1 \approx 1\%$ being the relevant values for the FRS, A_1 of each nuclear species in the RIB was calculated by β_1.

A_2 identification is more complicated because momentum changes and momentum spread increases after the secondary reaction. In order to measure $(B\rho)_2$ event by event, the dipole magnet ALADIN [7] and two one-dimensional position sensitive detectors GFI1 and GFI2 were employed. Each of them has an active area of 50×50 cm^2 and is composed of ∼500 scintillating fibers [8]. One end of each fiber is coupled to a position-sensitive photomultiplier. The position resolution is determined by the fiber width of 1 mm with an efficiency of 80 ∼ 100%. From the horizontal positions supplied by GFI1 and GFI2, together with the tracking detectors before ALADIN, $(B\rho)_2$ and then A_2 can be calculated [9].

For the determination of A_2 (as mentioned above) and scattering angle θ, the trajectories of the beam-like particles in front of and behind the target were measured by three two-dimensional position sensitive detectors ZST1, ZST2 and ZST3 which are two-stage multi-wire proportional chambers [10]. ZST1 and ZST2 have a size of 9×9 cm^2 while ZST3 has a size of 20×20 cm^2. The spatial resolution of ZST1 in both coordinates was 1.5 mm with 90% efficiency for Z≥ 8. ZST2 had a reduced efficiency of ∼50% for a spatial resolution of 1.5 mm. For ZST3, the resolution was 3 mm and the efficiency depended strongly on the charge number Z (e.g. 10% for Z = 8 and 75% for Z = 18). Because of this, for light particles, instead of ZST3, position information was derived from GFI1, GFI2 and the TOF-wall.

The neutron detector LAND [11] was employed to measure neutrons emitted in nucleon removal reactions and giant resonance decay [12].

Associated with the high beam energy, several experimental particularities must be taken into account. One is the large Doppler effect (Fig. 2). Gamma-rays emitted from projectiles which move with a velocity of $\beta \approx 0.6$ are strongly Doppler shifted. Compared with the γ-energy E_γ in the rest system which is associated to the projectile, the γ-energy E_γ^{lab} measured in the lab system is almost doubled for γ-rays emitted in forward direction ($\theta_\gamma = 0^o$) and only one half for those in backward direction ($\theta_\gamma = 180^o$) (Fig. 2a). Here θ_γ stands for the angle between γ-rays and the projectile. Because of the very small scattering angle of the reaction products, θ_γ is taken as the angle between γ-rays and the beam direction in order to simplify calculations. The uncertainty of θ_γ is given by the opening angle

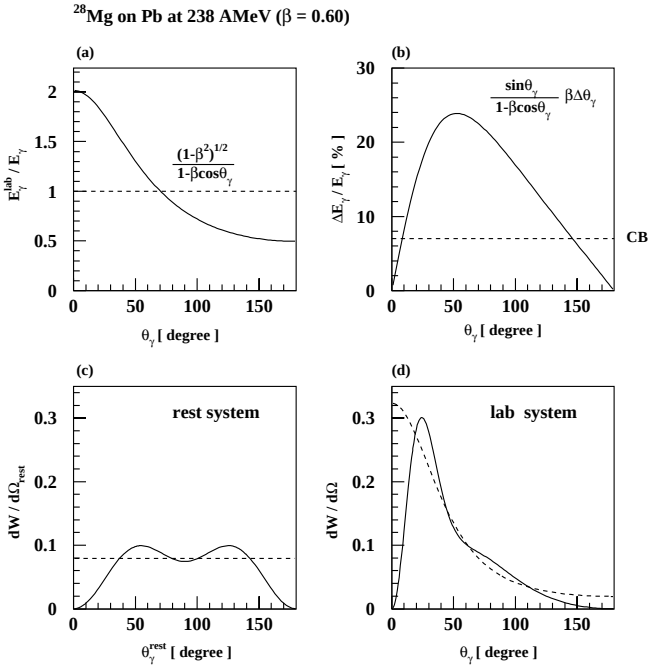

Fig. 2. (a) Doppler shift, (b) Doppler broadening for an opening angle of 18^o for one γ-detector element (the intrinsic energy resolution of the CB is marked by the dashed line), (c) isotropic (dashed line) and $2^+ \rightarrow 0^+$ (solid line) angular distribution of γ-rays in the rest system and (d) in the lab system (after Lorentz transformation). The integrated distribution is normalized to unity. The angular distribution of γ-rays in the lab system is peaked at forward angles where Doppler broadening is rather severe

of a γ-detector. For an opening angle of $\Delta\theta_\gamma = 18^o$ (given by the size of the individual CB-crystals), the corresponding spread of E_γ can be up to 20% at $\theta_\gamma \approx 55^o$ (Fig. 2b). To estimate the effect of the solid angle transformation on the measured intensity distribution, two extreme angular distributions of γ-rays in the rest system are considered in Fig. 2c. The dashed line represents a simple isotropic distribution, while the solid line displays a γ-ray angular distribution of a $2^+ \rightarrow 0^+$ transition after Coulomb excitation populating the magnetic sub-state $m = 0$ After Lorentz transformation, both distributions in the lab system are rather similar in the angular range accessible experimentally. Therefore the angular distribution in the rest system needs not to be accounted for when cross sections are determined from γ-intensities. From Fig. 2b and Fig. 2d, an average Doppler broadening of 15% is estimated as compared to the intrinsic energy resolution of the CB of 7%.

Another particularity is the very large atomic background due to radiative electron capture as well as primary and secondary Bremsstrahlung, which depends strongly on the beam energy and the nuclear charges of projectile and target [14,15]. The calculated energy distribution of the atomic background for a relativistic RIB on a Pb and C target is shown in Fig. 3 [16]. The cross section for Pb

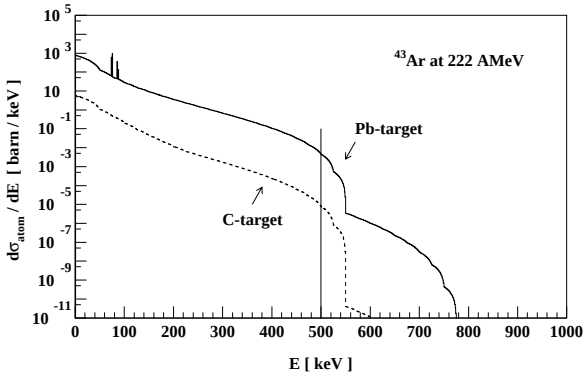

Fig. 3. The calculated energy distribution of the atomic background from ^{43}Ar ions of 222 A·MeV impinging on a Pb (solid line) and C target (dashed line). The 500 keV detection threshold used in the experiment is marked

is two orders of magnitude larger than for C because of its higher nuclear charge. In both cases, the cross sections are huge at low energies but decrease steeply as the energy increases and then drop at around 540 keV corresponding to the maximum electron knock-on energy available for secondary Bremsstrahlung ($E_{max} = 2\frac{\beta^2}{1-\beta^2} m_e c^2$). The integrated cross section of the atomic background is at least three orders of magnitude larger than typical Coulomb excitation cross sections. To suppress part of the low energetic atomic background, a 2 mm thick lead absorber was placed between target and the CB. Moreover, a threshold around 500 keV was chosen for the CB trigger. In addition, by requiring a minimal scattering angle θ or a neutron, events due to only atomic processes are suppressed.

Different nuclear reaction channels open at different impact parameter b, respectively scattering angle $\theta \propto \frac{1}{b}$ [12]. At $\theta \approx 0^o$, there is only elastic scattering. As θ is increased to $1 \sim 2^o$, Coulomb and nuclear excitation coexist. Increasing θ further so that the two colliding nuclei get into touch, few nucleon removal and fragmentation reactions take place with mass and charge change which can be identified by the A_2, Z_2 measurement. As an example, the cross sections for the excitation to the 2_1^+ state of ^{28}Mg using a Pb or C target were calculated by the coupled-channels calculation code CCNUC [17]. The known B(E2)$\uparrow$= 338.4 e^2fm^4 value [18] was used to calculate the Coulomb excitation. For the nuclear excitation, the optical potential was obtained in $t-\rho\rho$-approximation [19] at the present beam energy, using a nucleon-nucleon cross section of $\sigma_{NN} = 29.5$ mb and a real-to-imaginary ratio of the forward ($\theta = 0^o$) nucleon-nucleon scattering amplitude of $\alpha_{NN} = 0.6$. The nuclear deformation parameter β_2^N was assumed to be equal to the charge deformation parameter β_2^C, which was calculated from the known B(E2)$\uparrow$ value. The results are shown in Fig. 4 and Table 1. For the C target, the contribution from Coulomb excitation is negligibly small. For the Pb target, with an integration range of $0 < \theta < \theta_{max}$ (see Fig. 4 for the definition of θ_{max}) the total cross section is dominated by

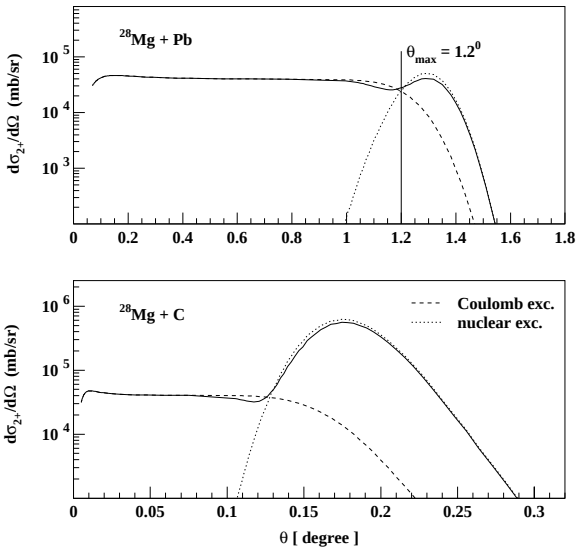

Fig. 4. The projectile angular distribution of the excitation cross section of the 2_1^+ state of ^{28}Mg when impinging on a Pb and C target at 238 A·MeV, obtained from coupled-channels calculations with CCNUC [17]. The dotted and dashed curves indicate the nuclear and Coulomb parts, respectively. The solid curve corresponds to the sum considering the interference term. The maximum scattering angle in the lab system θ_{max}, where nuclear and Coulomb excitation probabilities are approximately equal, is marked

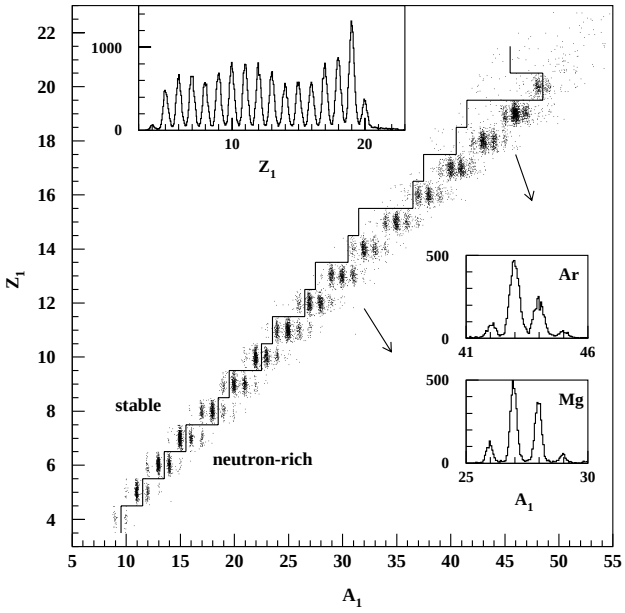

Fig. 5. The nuclear charge and mass distribution of the RIBs produced by fragmentation of a 330 A·MeV ^{50}Ti primary beam on a 4 g/cm^2 ^{9}Be production target with the FRS setting optimized to $A_1/Z_1 = 2.4$. The borderline between the stable and $\beta-$unstable nuclei is marked. On the top-left the Z_1 distribution is shown; on the bottom-right, as examples, the A_1 distributions of Mg and Ar are given

Table 1. The cross sections (in mb) integrated from Fig. 4. Here σ_C is the cross section for pure Coulomb excitation, σ_N nuclear excitation and σ_{C+N} the coherent sum

reaction, range of θ	^{28}Mg+Pb $(0,\theta_{max})$	^{28}Mg+Pb $(0,+\infty)$	^{28}Mg+C $(0,+\infty)$
σ_{C+N}	49.5	65.3	8.5
σ_C	51.3	56.6	1.1
σ_N	1.6	16.4	8.5

Coulomb excitation whereas for $0 < \theta < \infty$ the nuclear excitation amounts to about 25%. Therefore, if a scattering angle $\theta < \theta_{max}$ is required, nuclear contribution can be avoided and the cross section measured can be used to derive B(E2) values. However, at these high beam energies, the deflection angles are generally quite small and therefore the separation of Coulomb and nuclear excitation may be limited by the angular resolution of the position detectors. As the resolution in the present experiment was not sufficient, the contribution from nuclear excitation had to be estimated from the calculations of CCNUC which was checked to be reliable by a comparison with the cross section measured with the C target (see Table 2).

3 Beam "cocktail" and reaction products

The charge and mass distribution of the RIB delivered by the FRS in the selected A_1/Z_1 region is shown in Fig. 5. The spectrum on the top-left displays the Z_1 distribution showing a resolution of $\delta Z_1 \approx 0.5$. The two spectra on the bottom-right are the A_1 distributions of Mg and Ar (Z_1 =12 and 18) showing a resolution of $\delta A_1 \approx 0.3$ and 0.5 respectively. The efficiency to determine (Z_1, A_1) was ∼80%.

Using relativistic RIB, atomic processes, Coulomb excitation, nuclear excitation and nuclear reactions may occur. The probabilities for the former two processes are proportional to $\sim Z_t^2$ and are thus much stronger for a Pb target ($Z_t = 82$, $A_t = 208$) than for a C target ($Z_t = 6$, $A_t = 12$), while nuclear processes, being proportional to $\sim (A_1^{1/3} + A_t^{1/3})^2$, take place in both targets with more comparable probabilities (Z_t and A_t denote the nuclear charge and mass of the target).

Figure 6 shows the Z_2 distribution for incoming Mg isotopes (Z_1 =12). For $Z_2 = 5 \sim 11$ corresponding to proton removal reactions, the relative intensities are similar for both targets, whereas the intensity for $Z_2 = 12$ is nearly twice as high with the Pb- than with the C-target because of the much stronger Coulomb excitation with the Pb target.

To demonstrate the much larger probability of Coulomb excitation by Pb, the A_2 distributions of the Mg-isotopes after reactions of ^{28}Mg with a Pb and a C target are plotted in Fig. 7. The strong $A_2 = 28$ peak observed with the Pb-target is due to both Coulomb excitation and inelastic nuclear scattering(top). For a C target the Coulomb excitation is very small, therefore the relative intensity observed at $A_2 = 28$ is smaller (bottom). As the

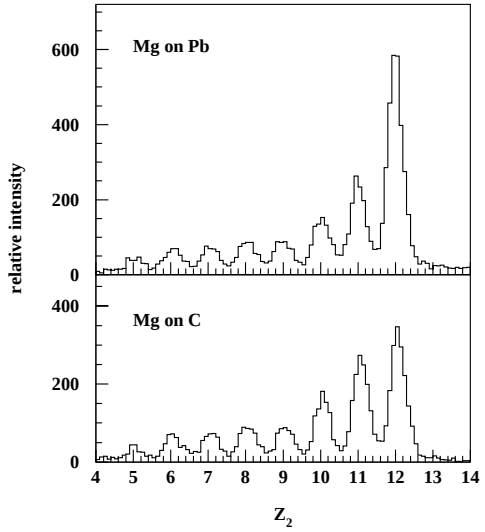

Fig. 6. The Z_2 distributions after reactions of Mg isotopes of ∼246 A·MeV with a Pb (top) and a C target (bottom), requiring $M_\gamma > 0$ and $E_\gamma > 1000$ keV to strongly suppress the atomic background

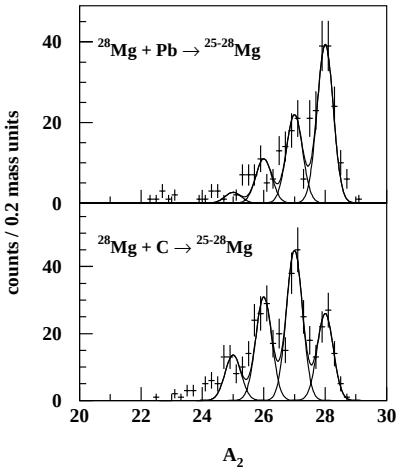

Fig. 7. The A_2 distributions after reactions of ^{28}Mg of 238 A·MeV with the Pb (top) and C target (bottom), requiring $Z_1 = 12$, $A_1 = 28$, $Z_2 = 12$, $M_\gamma > 0$ and $E_\gamma > 1000$ keV

nuclear processes in Pb and C cause a similar A_2 distribution, the Coulomb excitation contribution to the A_2 =28 peak observed with the Pb target can be estimated by subtracting a properly scaled A_2 distribution obtained with a C target. The ratio of the Coulomb excitation and nuclear processes strength in Pb is roughly derived as 2 : 1, which is consistent with the coupled-channels calculations given in Table 1.

The fragmentation products of the RIB with a C target are shown in Fig. 8, taking incoming ^{28}Mg and ^{43}Ar as examples. As a reference the two top spectra show the A_2 distribution of the beam obtained with the beam trigger

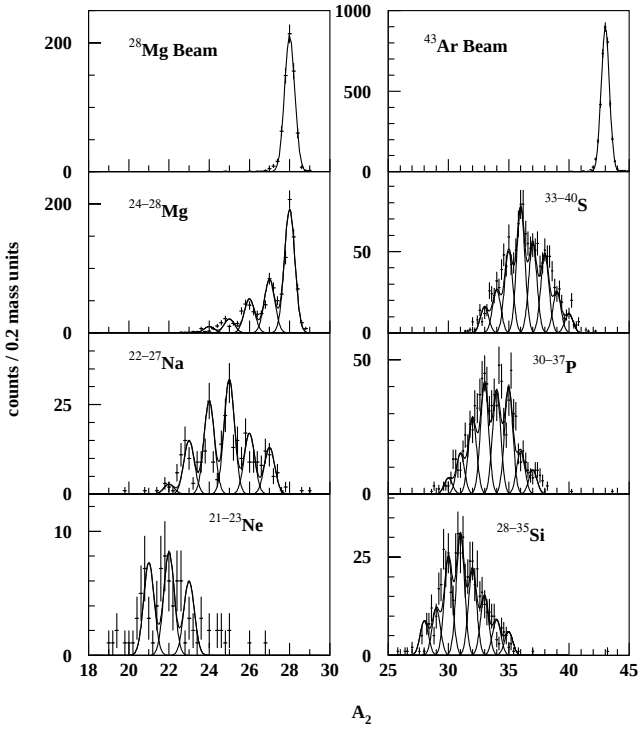

Fig. 8. top: The A_2 distributions of the ^{28}Mg and ^{43}Ar beams obtained with the beam trigger (see text for details); others: Fragment distributions after the reaction of ^{28}Mg (left) and ^{43}Ar (right) of 238 and 222 A·MeV with the C target. The A_2 resolution of the beam in the top spectra is used to fit the fragment distributions. There is no condition on the CB

gating only on atomic events. The resolution of A_2 for heavy nuclei like Ar was 0.8 mass units with an efficiency of 30%; for lighter nuclei like Mg, A_2 could be derived with a resolution of 0.8 mass units and an efficiency of 55%. The extracted experimental cross sections of these fragments are in good agreement with calculations using the empirical code EPAX [20,21].

By comparing Fig. 7 (bottom) and Fig. 8 (left-2nd.-top) one may notice that a condition of $E_\gamma > 1000$ keV has no influence on the relative intensities of the $^{25-27}$Mg fragments after the reaction of ^{28}Mg with the C target. This indicates that the fragmentation products are excited to states with energies higher than 1 MeV.

4 Gamma-spectroscopy

By gating on (Z_1, A_1) and (Z_2, A_2), individual in-beam γ-spectroscopy of more than 30 nuclear species in the RIB could be performed. The weakest channels like ^{42}Ar where discrete γ-lines were identified had an intensity of only ∼80 particles per second in the RIB [5]. As examples, γ-spectra from inelastic excitation of Mg-isotopes (Z_1 =12, A_1 =27, 28) with the Pb and C target, from the one neutron removal reaction of ^{43}Ar with the Pb target, as well

as from the one proton and one neutron removal reaction of ^{46}K with the C target will be discussed.

4.1 Inelastic excitation

Gamma-spectra from inelastic excitation of ^{27,28}Mg with the conditions (1) γ-multiplicity Mγ =1, (2) no signal from the neutron detector LAND, (3) $Z_2 = Z_1$ and (4) $A_2 = A_1$, are shown in Fig. 9, corrected event by event by the CB efficiency. No selection of the scattering angle θ was made, i.e. $0 \leq \theta \geq 30$mrad. Gamma-lines corresponding to the first excited states of ^{27}Mg ($5/2^+_1$ at 1698 keV and $5/2^+_2$ at 1940 keV) and ^{28}Mg (2^+_1 at 1473 keV) can be seen. The overall γ-resolution obtained is 20%. The two γ-lines of ^{27}Mg cannot be resolved. The atomic background is severe in the γ-spectra from the excitation with the Pb target while negligibly small with the C target. From the peak intensities in these spectra, the experimental cross sections can be derived. The uncertainties of the cross sections are mainly due to statistics.

Comparing the experimental cross sections with coupled-channels calculations (Table 2) employing the CCNUC code [17] and known B(E2) values, good agreement for ^{28}Mg (2^+) can be seen. The reason for the discrepancy in the odd nucleus ^{27}Mg is not well understood.

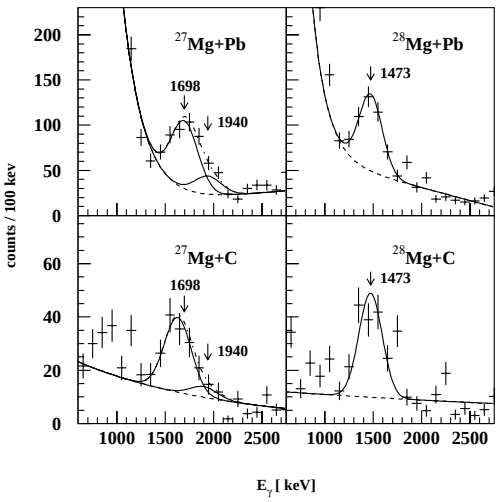

Fig. 9. Gamma-spectra from inelastic excitation of ^{27,28}Mg on Pb (top) and C (bottom), corrected for the CB efficiency. The structure in the ^{27}Mg case is fitted with two Gauss peaks because it is a mixture of two transitions in ^{27}Mg

Table 2. Cross sections σ_I^{cc} and σ_I^{exp} for excitation of state $|I\rangle$ obtained by coupled-channels calculations [17] and derived from experimental data

reaction	state $\|I\rangle$	σ_I^{cc}(mb)	σ_I^{exp}(mb)
^{27}Mg+Pb	$5/2^+_1$(1698) of ^{27}Mg	22.1	43.4± 9.1
^{27}Mg+C	$5/2^+_1$(1698) of ^{27}Mg	2.2	5.4± 1.5
^{28}Mg+Pb	2^+_1(1473) of ^{28}Mg	65.3	51.5±11.3
^{28}Mg+C	2^+_1(1473) of ^{28}Mg	8.5	8.1± 1.9

4.2 Nucleon removal reactions

In addition to inelastic excitation where single step processes are dominant and low-lying low-spin states are populated, nucleon removal reactions result in higher-spin states so that richer spectroscopic information can be obtained. Compared to inelastic excitation, the γ-multiplicity M_γ distribution of nucleon removal reactions is shifted to higher values as the reaction becomes more violent.

Gating on $Z_1 = 18$, $A_1 = 43$ and $Z_2 = 18$, $A_2 = 42$, the γ-spectra of the known nucleus ^{42}Ar after the one neutron removal reaction ^{43}Ar+Pb$\rightarrow{}^{42}$Ar*+1n are displayed in Fig.10. By requiring M_γ =1-4, a peak around 1200 keV which is related to γ-transitions in ^{42}Ar shows up (Fig.10: top). Because of the limited A_2 resolution and the much higher intensity of A_2=43, the cut on A_2=42 is contaminated by a A_2=43 component. If a neutron detected by LAND is required in addition to A_2=42, this component is suppressed and the spectrum quality is improved (Fig.10: bottom).

A key to obtain the most neutron-rich nuclides with still reasonable statistics was found by investigating proton removal reaction channels. For example, to study the very neutron-rich nucleus ^{44}Ar, the one proton and one neutron removal reaction from ^{46}K turned out to be superior to the one neutron removal reaction from ^{45}Ar because of their quite different intensities in the RIB (Fig.5). In addition, after proton removal reactions, the A_2 contamination from A_2=A_1 is not so severe (Fig.8) and it is therefore unnecessary to require neutron coincidence which would decrease the statistics further.

With the conditions $Z_1 = 19$, $A_1 = 46$ and $Z_2 = 18$, $A_2 = 44$, the one proton and one neutron removal reaction

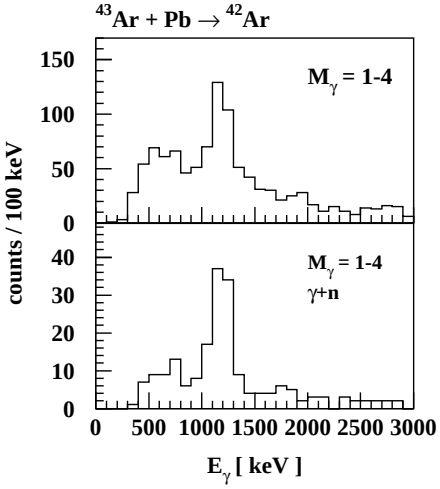

Fig. 10. The γ-spectra of ^{42}Ar after the one neutron removal reaction of ^{43}Ar impinging on the Pb target without (top) and with (bottom) neutron coincidence

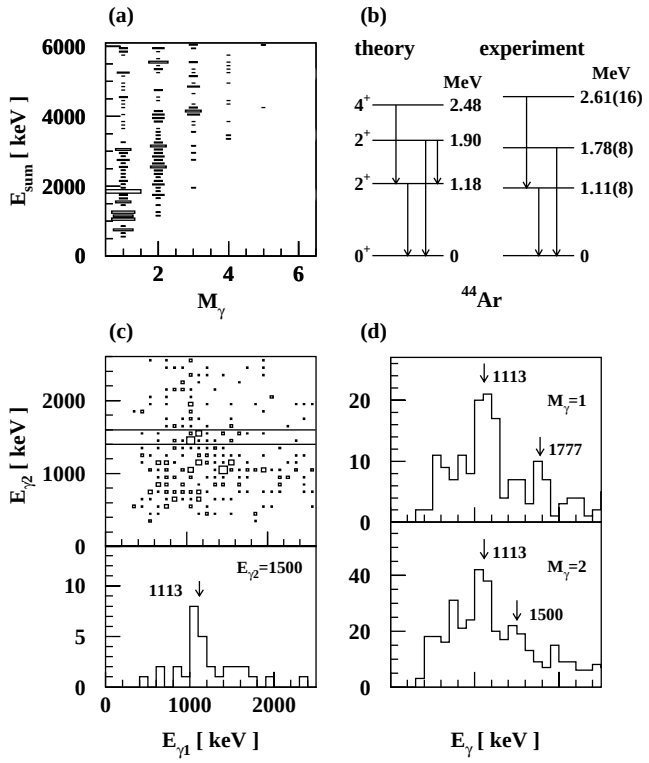

Fig. 11. Gamma-spectra from the nucleon removal reaction ^{46}K+C $\rightarrow ^{44}$Ar*+1n+1p and the derived level scheme of ^{44}Ar compared with shell model calculations [22,23]. See text for details

^{46}K+C$\rightarrow ^{44}$Ar*+1n+1p is investigated (Fig.11). From the sum energy E_{sum} vs. M_γ spectrum (a), one can see strong distributions at $M_\gamma = 1$, $E_{sum} = 1.1$ MeV and 1.8 MeV which indicate the first two excited states of ^{44}Ar and a structure at $M_\gamma = 2$, $E_{sum} = 2.6$ MeV which could be associated with a higher lying state.

The level scheme can be further confirmed by a γ-γ-matrix and single γ-spectra. In the γ-γ-matrix with M_γ =2 (c: top), a strong distribution at $\sim$ 1.1 MeV vs. 1.5 MeV can be seen. By setting an energy window around 1.5 MeV to one γ and projecting the other, a peak at 1.11 MeV shows up clearly (c: bottom), indicating a γ-cascade 2.61 MeV $\rightarrow$ 1.11 MeV $\rightarrow$ 0 in ^{44}Ar. In the single γ-spectra associated with different M_γ (d), with $M_\gamma = 1$, only transitions from the first two excited states to the ground state can be seen; with $M_\gamma = 2$, the transition from 2.61 to 1.11 MeV appears together with the transition from 1.11 MeV to the ground state.

As displayed in (b), the deduced level scheme of ^{44}Ar agrees well with the theoretical calculation in the framework of the shell model [22,23]. The calculation implies that the N = 28 closure persists even if a large neutron excess exists. The first excited state which was previously observed at MSU [24] could be confirmed, the other two states are new. The agreement with theory suggests a tentative assignment of the 1.78 MeV state to be the second 2^+ state and the 2.61 MeV state to be the first 4^+ state in ^{44}Ar.

5 Summary and outlook

The feasibility of a new experimental method – in-beam γ-spectroscopy with relativistic radioactive ion beams – has been demonstrated by studying the nuclear structure of the neutron-rich nuclei below ^{48}Ca with neutron number between the two magic numbers 20 and 28. Despite large Doppler broadening and huge atomic background, discrete γ-transitions could be observed in more than 30 nuclear species simultaneously, down to a beam intensity of only $\sim$80 particles per second.

Coulomb excitation experiments performed with intermediate-energetic RIB (below 50 A·MeV) at RIKEN [3] and MSU [1,24–26] gain from the much lower atomic background and larger scattering angle, enabling a better separation of Coulomb excitation from nuclear inelastic contributions. However, employing secondary fragmentation reactions to study higher excited states of exotic nuclei is superior at relativistic energies because of the thicker usable target and larger cross sections. Moreover, only at relativistic energies heavy ions are predominantly fully stripped, which is necessary for a proper selection of the reaction channels.

Since the experiment was performed, the available primary beam intensity at GSI has been improved by one to two orders of magnitude. Moreover, the advent of segmented Ge-detectors provides a γ-energy resolution of about 2% due to improved Doppler correction capabilities. Therefore the described method offers new opportunities to study exotic nuclei far from stability in the future.

This work was partly supported by BMBF and GSI.

References

1. T. Glasmacher et al., Annu. Rev. Nucl. Part. Sci. 48 (1998) 1
2. S. Wan et al., Z. Phys. A 358 (1997) 213
3. T. Motobayashi et al., Phys. Let. B 346 (1995) 9
4. V. Metag et al., Comments on Nucl. Part. Phys. 16 (1986) 213
5. S. Wan, PhD thesis, Universität Heidelberg, 1999
6. G. Stengel, Diplom thesis, Universität Frankfurt, 1996
7. ALADIN Collaboration, GSI Annual Report 1988, p. 292
8. J. Cub et al., Nucl. Instr. and Meth. A 402 (1998) 67
9. J. J. Livingood, The Optics of Dipole Magnets (Academic Press, New York and London, 1969)
10. H. Stelzer, Nucl. Instr. and Meth. A 310 (1991) 103
11. LAND Collaboration, Nucl. Instr. and Meth. A 314 (1992) 136
12. D. Schwalm, Coulomb Excitation at "Safe" and "Unsafe" Energies, MPIH-V 15-1994
13. H. J. Wollersheim, GSI Report, GSI-93-22. ISSN 0171-4546 (1993)
14. R. Anholt et al., Phys. Rev. Lett. 53 (1984) 234

15. R. Anholt et al., Phys. Rev. A 33 (1986) 2270
16. R. Holzmann et al., GSI Annual Report 1992, p. 48
17. C. A. Bertulani et al., Phys.Rev.C 53 (1996) 334
18. Nuclear Data Sheets, Edited by National Nuclear Data Center, Brookhaven National Laboratory, program ENSDAT
19. M. S. Hussein et al., Phys.Rep. 201 (1991) 279
20. K. Sümmerer et al., Phys. Rev. C 42 (1990) 2546
21. K. Sümmerer et al., 1999, submitted to Phys. Rev. C
22. J. Retamosa et al., Phys. Rev. C 55 (1997) 1266
23. F. Nowacki, private communication, 1998
24. H. Scheit et al., Phys. Rev. Lett. 77 (1996) 3967
25. T. Glasmacher et al., Phys. Lett. B 395 (1997) 163
26. R. W. Ibbotson et al., Phys. Rev. Lett. 80 (1998) 2081